Research article

A multiscale perspective on the kinetics of solid state transformations with application to bainite formation

Claas Hüter[1]**, Mingxuan Lin**[2]**, Diego Schicchi**[3]**, Martin Hunkel**[3]**, Ulrich Prahl**[2]**, and Robert Spatschek**[1,4,*]

[1] Max-Planck Institut für Eisenforschung GmbH, 40237 Düsseldorf, Germany
[2] RWTH Aachen University, Department of Ferrous Metallurgy, 52056 Aachen, Germany
[3] IWT Stiftung Institut für Werkstofftechnik, 28359 Bremen, Germany
[4] Forschungszentrum Jülich, Institute of Energy and Climate Research, 52425 Jülich, Germany

[*] **Correspondence:** Email: spatschek@mpie.de.

Abstract: We give an excerpt of recent developments in the experimentally benchmarked modeling of bainite formation in the press hardening process. As the press hardening process poses a heavily multi-parameter dependent modeling challenge, we focus on three main branches which complement each other. We emphasise the combination of basic sharp interface and phase field models with pragmatically adapted multi phase field models and experimentally parametrized implementations of the Johnson-Mehl-Avrami model. In the basic thermodynamic modeling part, we review fundamental aspects of displacive and diffusional-displacive transformations to predict dominant transformation morphologies. These results provide a link to multi-phase-field implementations which allow to simulate isothermal bainitic transformations, supported by available material data from thermodynamic databases. Excellent agreement with experiments, e.g. scanning electron microscopy for the transformed bainite in the high-carbon steel 100Cr6 shows the value of these model implementations. The further connection to Johnson-Mehl-Avrami models offers to extend the understanding to transformation plasticity for the press hardening steel 22MnB5.

Keywords: bainite formation; press hardening; phase field modeling; elasticity; transformation plasticity

1. Introduction

The discovery of bainite by Bain in 1930 [1] rose global interest due to the very attractive combination of strength, toughness and fatigue properties. In spite of its industrial relevance, the fundamental dispute whether bainite formation is mainly displacive, diffusive or both remains unsolved [2]. The

formation of bainite requires the displacive transformation of austenite into supersaturated bainite, carbon diffusion into the austenite and the diffusion controlled formation of carbides. If the displacive process controls the transformation, it is expected that bainite nucleation, similar to martensite, governs the process. If diffusion limits the transformation, the bainite growth is expected to exhibit a growth mechanism comparable to those observed in Widmanstätten ferrite formation. Investigations corresponding to the former perspective on bainite formation [3, 4, 5, 6, 7] often anticipate autocatalytic nucleation, while research conducted in the spirit of the latter perspective is typically based on Johnson-Mehl-Avrami-Kolmogorov models [8, 9].

As described in [7], the autocatalytic nucleation shows a clear dependence on the prestrained state of the austenite, and additional stresses lead to an acceleration of the bainite formation [10, 11]. Apart from the activation of intergranular nucleation sites due to pre-transformation strain and applied stresses, also the size of the bainite units changes drastically under large stresses [12, 13, 14], and the bainite needle orientation is stress dependent as well [15]. Additionally, it has been found for a medium carbon steel that large stresses change the orientation via variant selection [16] and prestrained austenite leads to much finer bainite [17, 7]. Furthermore, the bainite phases show increased strength due to a higher carbide density, and similar effects were found also in the press hardening steel 22MnB5 [18, 19].

Press hardening is one of the key production technologies for high strength steels specifically in the automotive industry [20]. Parts as A- and B-pillars, roof rails or bumpers are fabricated using production facilities based on this method. Currently, it is of specific interest to further develop advanced process technologies based on press hardening, where bainitic press hardening is one of the most promising candidates. This method, using a combination of interrupted cooling and quasi-isothermal holding in the bainite region, offers extremely attractive strength-failure-strain combinations [21]. In general, controlling the process tool temperature partially (partial press hardening) offers a vast amount of possible advances in process technology which can yield work pieces with locally varying thermoelastic properties for a wide range of applications, known as tailored tempering.

Apparently, such advanced concepts of steel design require the solution of various theoretical challenges accompanying this promising class of materials. The resulting microstructure, which can be obtained with such tailored tempering methods, exhibits a huge variety of complex process dependencies. One example for these intricate aspects of the specific material behavior is the prediction of transformation plasticity in quenching from the prestrained austenite phase. In the case of 22MnB5 press hardening, the process demands a quenching within 5-10 seconds for the transformation from the austenite to martensite, where the mechanical properties are mainly controlled by the carbon and boron content, while manganese and chromium have minor influence only on the final strength. The transformation plasticity, which appears during the rapid quenching, then needs to be controlled in agreement with the process-determined requirements, while the transformation from the prestrained austenite shows an elasto-plastic response to the applied stresses depending strongly on the precise strain state of the austenite. Also, the transformation plasticity in a post-yield-strength regime exhibits a strong influence on the applied stresses which are modified due to internal stresses. This specific part of the entire process chain exhibits the need for a scale bridging description coupling thermochemical and mechanical modeling.

Consequently, the approaches pursued to tackle the problem cover calculations performed with various different methods. On the smallest scale, where a basic thermodynamic description is clearly

available, phase field models [22, 23] are an established tool to connect the morphology selection understanding obtained from sharp-interface descriptions to extended mesoscale regimes. More sophisticated phase field implementations as the multi-phase-field model used in the software MICRESS [24] allow the connection to process specific environmental conditions and material specific thermodynamic data. To capture the lath-like morphology of ferrite formed by displacive mechanism, many models assign anisotropic interfacial mobility and energy to the ferrite-austenite phase boundary. The resulting shape of the phase boundary comprises several facets which are kinetically or energetically favored. Loginova et al. [25] simulated the 2D growth of Widmanstätten ferrite and obtain a morphology similar to the realistic microstructure. A related approach has been applied by Song et al. [26, 27] to the simulation of bainitic transformation in a 100Cr6 steel. Some other extended phase field models introduce a certain form of mechanical energy into the free energy functional. Arif and Qin [28, 29, 30] employed an approximated formula for the strain energy of each bainitic sub-unit proposed by Bhadeshia [31]. They also introduced autocatalytic nucleation of neighboring sub-units to simulate the growth of a complete bainite sheaf. In more sophisticated models, the mechanical response of both austenite and ferrite is also resolved by linear elastic [32] or elasto-plastic [33, 34, 35] models. An elasto-plastic phase-field model was developed by Kundin et al. [33, 34] using the crystal plasticity framework [36]. The model is then applied to explore the interaction of the martensitic transformation with dislocation evolution.

To take into account process-specific complex plasticity phenomena on larger scales, finite element calculations on top of Johnson-Mehl-Avrami-models are an established method [37, 38, 8]. There are numerous papers dealing experimentally with the transformation plasticity for the bainite formation under small stresses [10], meaning stresses below half of the yield strength of austenite. Under these conditions, the transformation plasticity depends linearly on the stress. However, for higher stresses the transformation plasticity can be strongly nonlinear. During press hardening the transformation plasticity is responsible for a small spring-back compared with conventional cold or hot forming [39, 40, 41].

The present article intends to give an overview on several aspects mentioned above, starting from fundamental theoretical concepts, via phase field simulations of bainite formation, to macroscopic plastic effects during bainitic press hardening. It is organized as follows.

Section 2 briefly summarizes the materials and methods used for the work in this article. The central results and their discussion is contained in section 3. In detail, the analysis of the transformation processes from a fundamental thermodynamic perspective is developed in section 3.1. A further theoretical treatment of solid-solid transitions in the displacive and the diffuse-displacive regime is given in section 3.2. The onset of displacive transformations is described in terms of a Griffith-like elastic growth criterion, and the dominance of appearing morphologies is distinguished both by sharp interface predictions of the growth velocity and phase field simulations concerning the stability of the growth modes. The inclusion of diffusional transport as governing mechanism for the transformation also yields a strong dependence of the diffusional transformation on the relative orientation of growth direction and lattice strains.

In section 3.3 we develop our phase field approach to account for available thermodynamic material data to provide more insights into the modeling of bainite transformation. We focus on the high carbon steel 100Cr6 and simulate the microstructure evolution during an isothermal bainite transformation, starting from a sample which is austenitized at higher temperature. Here, the emphasis is on the carbon

redistribution in the austenitic matrix. The results obtained here transfer the basic thermodynamic description to the process-governed environmental conditions required for the detailed understanding of the entire transformation. At this level the role of transformational plasticity is not yet accounted for, and we describe the approach to this aspect of the process in section 3.4.

In section 3.4 the focus is on the influence of high stresses, i.e. beyond the austenite yield strength, on the bainitic transformation in a 22MnB5 steel. Experimental and finite element simulations regarding the kinetics of the bainitic transformation are presented. The study is based on a Johnson-Mehl-Avrami model and shows the strong dependence of the transformation speed and the strain states on the applied stress. A strong nonlinearity of the anisotropic strain response to stresses has been found in the longitudinal and thickness directions, beginning in the range between 50-100 MPa, where the austenite yield strength is located for the relevant temperatures.

The different aspects of the article are summarised in Section 4, with an outlook to future activities to bring the different levels of modeling together.

2. Materials and Method

The work in this article is based on both experimental and theoretical work.

On the experimental side, flat tensile samples were performed in a servo-hydraulic deformation dilatometer. The specimens are quenched to 500°C after austenitization and held for 20 minutes. Length and width changes are determined by a laser extensometer. As materials the press hardening steel 22MnB5 and the high carbon steel 100Cr6 are used.

On the theoretical side, various methods were used, starting from thermodynamics, including linear elasticity. Sharp interface formulations are used to express the microstructure evolution equations for diffusionless and diffusion limited processes. Proper phase field methods are used for more flexible and convenient formulation, being employed for the simulations. The phase field code MICRESS is used for the simulation of bainite formation, including a coupling to ThermoCalc databases for free energy curves. On the macroscopic level Johnson-Mehl-Avrami models are used to describe the transformation kinetics.

For further details we refer to the following sections.

3. Results and Discussion

3.1. Thermodynamic aspects

In this section we inspect several aspects of the equilibrium properties of solid state transformations. Since the focus of this section is to gain generic insights, we use simplified models to illustrate fundamental concepts. This means that we restrict ourselves for the purpose of clarity to elastic deformations and do not consider plastic effects. This constraint will be released in section 3.4. Moreover, we use only linear elasticity, and more specifically only isotropic linear elasticity. This has the advantage that one needs only two elastic constants, and for further simplification we assume that they are identical in all phases. These assumptions have central consequences: First, without the anisotropy in the elastic constants there is no preferred spatial orientation. Nevertheless, anisotropy can still be induced by transformation strains. As we will see in detail in the following, this effect is important, as for the diffusion limited processes only this aspect leads to selection of microstructure scales and transformation

velocities. It is therefore important to understand the role of fundamental symmetries starting from the most symmetrical situation of isotropic elasticity. In Section 3.3 we will then generalise the developed concepts to bainitic transformations. This will require in particular to use anisotropic formulations, which we leave out here for clarity.

We begin the analysis of the transformation processes from a thermodynamic perspective. In an isothermal situation we consider the transition of a metastable phase, which we will in the following denote as γ phase into a more stable phase α. These two phases could for example be the austenite γ and the bainitic ferrite α of an iron based alloy. For the moment we ignore concentration variations inside the phases, as we first have displacive transformations in mind, which are controlled by the interface kinetics. However, the following considerations are of thermodynamic nature and serve as a background for the model formulation steps in the following sections.

In the framework of the approximations mentioned above the free energy densities of the two phases are

$$f_\gamma \quad = \quad f_\gamma^0 + \frac{1}{2}\lambda\epsilon_{ii}^2 + \mu\epsilon_{ik}^2, \tag{1}$$

$$f_\alpha \quad = \quad f_\alpha^0 + \frac{1}{2}\lambda(\epsilon_{ii} - \epsilon_{ii}^0)^2 + \mu(\epsilon_{ik} - \epsilon_{ik}^0)^2. \tag{2}$$

Here, f_γ^0 and f_α^0 are the free energy densities without the elastic effects. They contain the concentration and temperature dependence and can be taken from thermodynamic databases, as will also be explained in more detail later. λ and μ are the Lamé constants. The strain ϵ_{ij} is related to the displacements u_i according to $\epsilon_{ij} = (\partial_j u_i + \partial_i u_j)/2$. We consider the γ phase as reference state, hence the stress free eigenstrain does not appear here. In contrast, for the α phase it is expressed through ϵ_{ij}^0. If we ignore tetragonal distortions, we can use an isotropic approximation, $\epsilon_{ij}^0 = \epsilon\delta_{ij}$, where the quantity ϵ will in general depend on the structural change between the phases, concentration differences e.g. of carbon, but also on temperature effects. For sufficiently fast diffusion and small concentration gradients we can therefore take ϵ as a constant material parameter for a given temperature. In the following we proceed with this diagonal eigenstrain and will look at more general situations later.

For the solution of the elastic problem we need to consider specific geometries. In view of later applications to press hardening processes the situation of given volumetric constraints, i.e. prescribed displacements at the sample boundaries, is of special interest. We consider a strip like geometry (see Fig. 1), where at the upper and lower boundary of the strip displacements shall vanish, $u_i = 0$. In perpendicular direction z the sample is assumed to be thick, such that a plain strain assumption, $u_z = 0$, $u_x = u_x(x, y)$ and $u_y = u_y(x, y)$ is legitimate. We assume that the constraints at the boundary are chosen such that the pure parent γ phase is stress free. We expect later in a dynamical situation the α phase to invade the γ phase in the direction of the sample, as depicted in Fig. 1. This will be the case if the thermodynamic driving force, which is related to the difference $f_\gamma^0 - f_\alpha^0$ is sufficiently high. Far ahead of the growing front the material is stress free, hence the energy density is f_γ^0 there. Behind the tip, we usually find a two-phase configuration, which is homogeneous far away. This implies that the only non-vanishing strain component is there ϵ_{yy}, which is different in the two phases, but spatially homogeneous in each of them. The volumetric constraint of given displacement at the upper and lower surface of the sample implies the "lever rule" $(1 - \chi)\epsilon_{yy}^\gamma + \chi\epsilon_{yy}^\alpha = 0$, where χ is the volume fraction (which is formally equivalent to a driving force) of the α phase in the tail region. Equilibrium demands that the free energy per area, $\mathcal{F} = (1 - \chi)f_\gamma + \chi f_\alpha$ is minimised with respect to the degrees of freedom
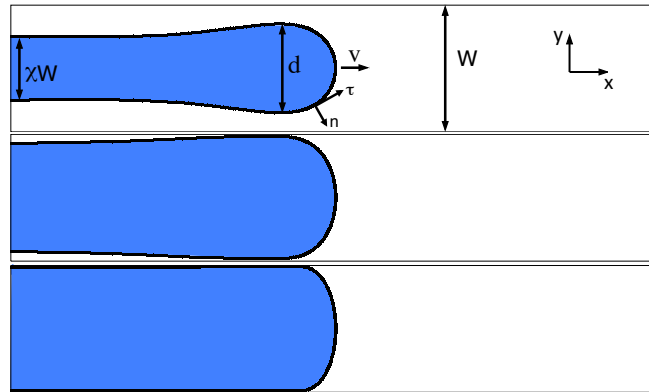
Figure 1. The single crystal fingered geometry in the steady state regime, calculated with the phase field approach for three values of the driving force $\chi = 0.5$ (top) and $\chi = 0.85$ (centre), $\chi = 1.05$ (bottom), with Poisson ratio $\nu = 1/3$ and $W/W^\star = 10$. For further details we refer to [42].

χ and ϵ_{yy}^α. The latter condition is equivalent to a stress balance at the interface between α and γ. From this we obtain the equilibrium volume fraction of the α phase in the tail,

$$\chi = \frac{1-2\nu}{1+\nu}\left[\frac{1-\nu}{E\epsilon^2}(f_\gamma^0 - f_\alpha^0) - 1\right], \tag{3}$$

where we expressed the elastic properties here through the Young's modulus $E = \mu(3\lambda + 2\mu)/(\lambda + \mu)$ and the Poisson ratio $\nu = \lambda/[2(\lambda + \mu)]$. This result is in agreement with the interpretation of $f_\gamma^0 - f_\alpha^0$ being the nonelastic driving force for the transformation. If it is high, the volume fraction χ reaches (and exceeds) unity, and then the γ phase is completely converted into the α phase. Below, but above a threshold value discussed next, we obtain a two-phase state, which is stabilised by the mechanical constraint at the boundaries. In fact, the volume fraction χ depends linearly on the "temperature" $f_\gamma^0 - f_\alpha^0$. The concentration vanishes below a threshold value

$$(f_\gamma^0 - f_\alpha^0)_{\text{nuc}} = \frac{E\epsilon^2}{1-\nu}. \tag{4}$$

It expresses the elastic nucleation threshold: The formation of a two-phase region with coherent phases induces elastic stresses, which cost energy and therefore counteract phase separation. The above "driving force" $(f_\gamma^0 - f_\alpha^0)_{\text{nuc}}$ needs be be exceeded to trigger the phase transformation. We point out that this elastic nucleation barrier is a bulk term and must not be confused with an interfacial term, which prevents spontaneous nucleation. Interfacial energy has not yet been taken into account; this will follow in the next steps. We also mention that the above expression for the elastic nucleation barrier is not restricted to our specific geometry and boundary conditions. It appears generically in isotropic situations with equal elastic constants for coherent nucleation in the bulk due to (diagonal) volumetric mismatches ϵ_{ij}^0 according to the Bitter-Crum theorem [43]. For the specific situation, which we consider here, the "temperatures" $f_\gamma^0 - f_\alpha^0$, at which χ reaches zero and one, can be considered as start and

finishing temperatures of the transformation, respectively. We note that the volume fractions for the reverse transformation will be the same. This is a particular feature of the effect that the eigenstrain ϵ appears only quadratically in the expressions for this purely elastic case.

To judge the possibility of a phase transformation we also need to consider the free energy change. Only if the free energy decays during the process, the transformation will proceed as anticipated, otherwise the tip of the α phase will convert back to the γ phase. From the difference between the free energy ahead of the tip and in the tail (both far away from the advancing front) we get

$$\Delta F := W(f_\gamma^0 - \mathcal{F}) - 2\gamma_s = 2\gamma_s \left(\frac{\chi^2}{\chi_W^2} - 1 \right), \tag{5}$$

where we introduced the abbreviation $\chi_W^2 = W^*/W$ with

$$W^* = \frac{4(1 - 2\nu)(1 - \nu)\gamma_s}{E\epsilon^2(1 + \nu)}, \tag{6}$$

and the asymptotic phase fraction χ is given by Eq. (3). We have additionally taken into account the interface energy γ_s. In the rear, we have two interfaces, hence an additional energy contribution $2\gamma_s$ appears there. Growth of the α phase is possible for $\Delta\mathcal{F} > 0$ or equivalently $\chi > \chi_W$. This is a stronger condition than the above nucleation threshold $\chi > 0$. It is equivalent to the Griffith condition for crack growth, which is also a result of the balance of bulk elastic and interfacial effects [44, 45].

We can also consider more complex transformation strains, in particular involving shear components. This can for example occur in hexagonal-orthorhombic transitions in ferroelastic materials [46]. We inspect the transformation in the basal plane, where the transformation induces a symmetry reduction from C_6 of the γ phase to C_2 for the α phase. The new phase can appear in three variants, and the transformation strains are given by

$$\epsilon_{xx}^0 = -\epsilon_{yy}^0 = \epsilon \cos 2\theta, \quad \epsilon_{xy}^0 = \epsilon \sin 2\theta, \tag{7}$$

and all other eigenstrain components vanish. The angle θ can take here the three discrete values 0 and $\pm 2\pi/3$. A possible scenario is the formation of a single variant of the α phase. However, this induces a strong shear strain in the tail region and is therefore energetically unfavorable from an elastic bulk perspective. Instead, the formation of twin structures consisting of different variants, as depicted in Fig. 2, is favorable, as then the shear strains cancel each other. This is also verified by a comparison of the elastic energies in the spirit of Eq. (5) for the different microstructures. For the bicrystal configuration the volume fraction of the α phase is asymptotically analogous to Eq. (3)

$$\chi = \frac{1}{1 - 2\nu} \left[\frac{4(1 - \nu^2)}{E\epsilon^2}(f_\gamma^0 - f_\alpha^0) - \frac{1}{2} \right]. \tag{8}$$

The energy gain is still expressed through Eq. (5) with the replacement

$$W^* = \frac{8(1 - \nu^2)(2\gamma_s + \gamma_{gb})}{(1 - 2\nu)E\epsilon^2}. \tag{9}$$

Here, additionally to the interfacial energy between α and γ also the grain boundary energy between the different variants of the α phase, γ_{gb}, appears. From an energetic perspective we cannot distinguish
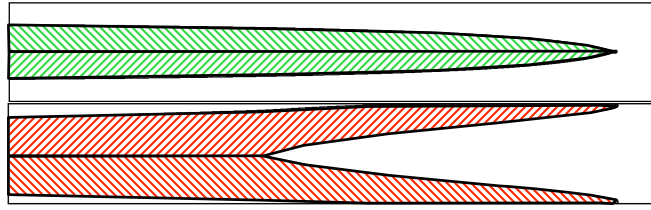
Figure 2. Simulated bicrystal patterns calculated at $W/W^\star = 5$. The figure shows the tip region in the steady state regime. Forward slashes correspond to $\theta = -2\pi/3$, backward slashes to $\theta = 2\pi/3$. For $\chi = 0.6$, we find the growth velocities $v/v_0 = 1.14$ (top) and $v/v_0 = 0.48$ (bottom), hence the single tip arrangement is kinetically preferred. For further details we refer to [42].

between the different microstructures shown in Fig. 2, which differ only by an exchange of the variants $\theta \to -\theta$. In the tail region they fill the same volume fraction, and therefore the global free energy difference as driving force for the process is the same. Nevertheless, as will be shown in the next section, there can still be differences in the growth kinetics, which therefore prefers one of the growth modes.

So far, we have only looked at the asymptotic regions far away from the transformation front. At the front itself equilibrium demands for stationary fronts the condition

$$\tilde{f}_\gamma - \tilde{f}_\alpha - \gamma\kappa = 0, \tag{10}$$

with the local interface curvature κ in a sharp interface picture. Moreover, instead of the bare free energy densities modified expressions appear, given by

$$\tilde{f} = f - \sigma_{nn}\epsilon_{nn} - 2\sigma_{n\tau}\epsilon_{n\tau}, \tag{11}$$

where we assumed here in accordance with the above analysis a plain strain situation. The direction n and τ are local interface normal and tangential directions, as depicted in Fig. 1. The additional contributions, which affect the local energy balance (10) are due to the coherency between the phases. If one phase is converted to the other, closing of the mismatch between the phases to maintain coherency requires mechanical work, as expressed through the additional terms in Eq. (11). For an extended discussion of this issue we refer to [42, 47, 48]. We can therefore conclude that Eq. (10) expresses the absence of an energy gain as local driving force for a conversion of one phase into the other.

3.2. Influence of strain on the kinetics of displacive and diffusional-displacive transformations

Whenever we have a disbalance of energy in the spirit of a violation of Eq. (10) at an interface point between the different phases, kinetics will lead to front propagation in order to reduce the total free energy. In this section we inspect such situations both for diffusionless and diffusion-limited transformations as limiting cases. Also, we introduce both sharp interface and phase field formulations to simulate these microstructure evolution processes.

3.2.1. Displacive transformations

In the framework of linear non-equilibrium thermodynamics we therefore expect as local equation of motion for solid-state transformations which are limited by interface kinetics,

$$v_n = \bar{\mu}_{\alpha\gamma}(\tilde{f}_\gamma - \tilde{f}_\alpha - \gamma\kappa), \tag{12}$$

where v_n is the local interface normal velocity in a sharp interface description and $\bar{\mu}_{\alpha\gamma}$ the interface mobility. For the sake of simplicity we assume it to be isotropic here, and generalisations will be considered in the next section. Equation (12) anticipates that the front velocity is determined by the kinetics of the interface, i.e. the structural reorganization from one phase to the other. The modified free energy densities $\tilde{f}$ will in general depend also on the local composition, but in the spirit of a diffusionless process we assume that it is fixed on the timescale of the interface motion. This implies that the front propagation can be much larger than for diffusion limited processes, such that even inertial effects can play a role. In contrast, the equation of motion for diffusion limited processes is later given by Eq. (20), and depends explicity on the diffusive fluxes into the moving interface. Close to the Griffith threshold we expect the steady state front velocity to be linear in the effective driving force, hence

$$\frac{v}{v_0} \sim \chi - \chi_W, \tag{13}$$

with a velocity scale $v_0 = 2\bar{\mu}_{\alpha\gamma}\gamma_s/W^\star$ in the single crystal geometry with hydrostatic lattice strains, and $v_0 = 2\bar{\mu}_{\alpha\gamma}(2\gamma_s + \gamma_{gb})/W^\star$ in the bicrystal geometry with a shear transformation.

Whereas such a sharp interface description is feasible and useful for theoretical inspections, a proper phase field formulation is useful for generalisations of the model and complex morphologies. We illustrate this here for the isotropic eigenstrain, as we have to distinguish only between two phases and not between variants of the secondary phase. This allows to discriminate the two phases by a single order parameter ϕ, which we normalise to be $\phi = 1$ in the γ and $\phi = 0$ in the α phase. The generating free energy functional for the phase field evolution equation is given by

$$F = \int \left(f_\gamma\phi + (1 - \phi)f_\alpha + f_s + f_{dw} \right) dV \tag{14}$$

with the gradient square term

$$f_s = \frac{3\gamma_s\xi}{2}(\nabla\phi)^2 \tag{15}$$

with the interface thickness parameter ξ and the double well potential

$$f_{dw} = \frac{6\gamma_s}{\xi}\phi^2(1 - \phi)^2. \tag{16}$$

Alternatively, for the latter also a double obstacle potential can be chosen, and this is demonstrated in the following section. We note that for the bulk energy terms the original free energy densities, as given by Eqs. (1) and (2) are used, without the coherency modification (11). The reason is that in a phase field approach, where the displacement field is considered as basic quantity, which is continuous in the entire simulation domain, satisfies coherency at the interfaces automatically. This issue has been discussed in detail in [47]. With this, the phase field evolution equations are given by

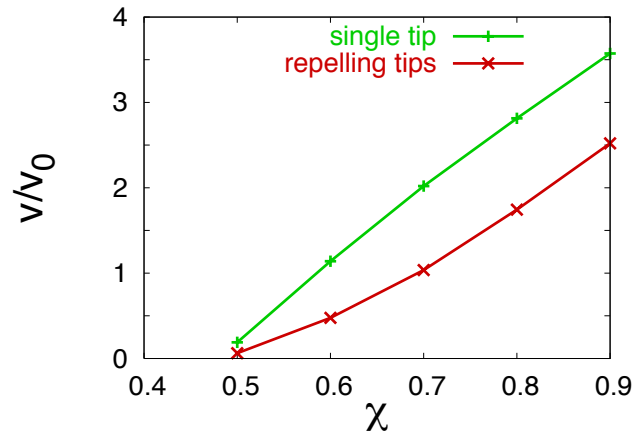$$\frac{\partial\phi}{\partial t} = -\mu_{\alpha\gamma}\frac{\delta F}{\delta\phi}. \tag{17}$$

Figure 3. Steady state velocity v as function of the thermodynamic driving force, expressed here through the α phase volume fraction far behind the advancing front. The bicrystal pattern shows a clear preference for the single tip morphology. The colour coding corresponds to Fig. 2. We use here $W/W^{\star} = 5$. For further details we refer to [42].

This evolution equation is equivalent to the sharp interface picture (12), provided that the interface thickness is small in comparison to the physical length scales, if we identify $\mu_{\alpha\gamma} = \bar{\mu}_{\alpha\gamma}/3\xi$. We note that the phase field serves as (mathematical) order parameter, which has a sharply localized gradient only in the interface. Hence the above equation of motion must not be confused with a diffusion equation, which typically leads to long tails in the concentration profiles in difffusion limited processes. The equivalence of the phase field representation (17) to the diffusionless interface kinetics (12) can be obtained by a sharp interface analysis [47]. Additionally, we have the mechanical equilibrium condition

$$\frac{\delta F}{\delta u_i} = 0. \tag{18}$$

For fast processes the extension to dynamical elasticity is straightforward and has been discussed in [42]. Examples for the obtained microstructures in the steady state regime are shown in Fig. 1. This example demonstrates how to link sharp interface and phase field descriptions for displacive solid-state transformations.

For the transformations involving shear, which lead to bicrystal patterns, require in general to distinguish also the variants and to introduce the twin boundary energy, which can be realized using multi-order parameter phase field models, and this will be explored in the following section. For small grain boundary energies $\gamma_{gb} \ll \gamma_s$ we can invoke symmetry along the plane $y = 0$ and proper boundary conditions for the phase field to reflect the correct contact angles at the triple junction. This allows to describe the dynamics with only minor modifications of the above single-order parameter phase field model, as explained in more detail in [42]. The resulting microstructures are shown in Fig. 2, depending on the layering of the variants. The two twin structures with a single or two separate tips differ in the steady state velocity, as shown in Fig. 3. Altogether, these examples show that the combination of sharp interface, phase field and thermodynamic modeling allows to obtain important insights into the statics and dynamics of displacive solid-state transformations. The analytic predictions are most useful

in simple geometries and provide exact predictions for asymptotic regions. The phase field simulations are more flexible concerning complicated patterns than sharp interface implementations. Further examples of phase field models for more complex interactions of microstructure and free interface evolution in martensitic transformations can be found e.g. in [49, 50, 22, 23]. Applications to bainite formation will be discussed below in Section 3.3.

3.2.2. Diffusion-limited transformations

Pearlitic or bainitic transformations are examples for diffusional or mixed diplacive-diffusional solid-solid transitions which are strongly influenced by elastic effects. The coupling of displacive and diffusional transitions has been investigated recently emphasising engineering aspects, see [32, 51], and will also be discussed in the next section. In order to separate these effects for a fundamental understanding, we continue with the discussion of diffusional transformations alone.

An overview of diffusional transformations with elastic effects can be found e.g. in [52, 49, 22]. We focus here on situations with coherent interfaces [36, 42, 47, 53, 54]. As for displacive transformation studies, the combination of classical sharp interface descriptions and phase field modeling turns out to be a fruitful approach. Central aspects are related to the interaction of diffusive transport, transformational lattice strains, grain boundaries and triple junctions. Component diffusion will be considered in Section 3.3, and here we complementary discuss the effect of heat diffusion and its absorption and release at propagating phase fronts.

In a dimensionless formulation we introduce $w = c_P(T - T_\infty)/L$, where T is the local temperature, c_P the specific heat capacity, L the latent heat for the $\gamma - \alpha$ transition, and T_∞ is the temperature in the γ-phase far away from the interface. The heat diffusion in the bulk is described by

$$\frac{\partial w_{\alpha,\gamma}}{\partial t} = D\nabla^2 w_{\alpha,\gamma} \tag{19}$$

for both phases, with the thermal diffusivity D, which we assume to be the same for α and γ. Heat conservation at the interface demands

$$v_n = D\vec{n} \cdot (\nabla w_\alpha|_{int} - \nabla w_\gamma|_{int}) \tag{20}$$

with the interface normal vector $\vec{n}$ as in Fig. 1. The two gradients are evaluated right at the interface, therefore their normal components express the heat flux into or away form the interface on both sides. Local equilibrium implies that the temperature at the interface is essentially equal to the phase coexistence temperature T_{eq}, apart from curvature and elastic modifications,

$$w_{\alpha|int} = w_{\beta|int} = w_{|int} = \Delta - d_0\kappa + T_{eq}c_P\delta f^{el}/L^2 \tag{21}$$

with the capillary length $d_0 = \gamma_s T_{eq}c_P/L^2$, and the dimensionless undercooling is given by $\Delta = c_P(T_{eq} - T_\infty)/L$. The elastic contribution δf_{el} depends on the underlying model. For a transformation as defined through Eqs. (1) and (2) we get

$$\delta f^{el} = \sigma_{ik}^0 \epsilon_{ik}^{(\gamma)} - \frac{E\left[(\epsilon_{\tau\tau}^0)^2 + (\epsilon_{ss}^0)^2 + 2\nu(\epsilon_{\tau\tau}^0)(\epsilon_{ss}^0) + 2(1-\nu)(\epsilon_{s\tau}^0)^2\right]}{2(1-\nu^2)}, \tag{22}$$

where in a three dimensional case we have two local tangential directions τ, s at the interface. This expression therefore involves projections of the stress free strain tensor ϵ_{ij}^0 into the local coordinates, as
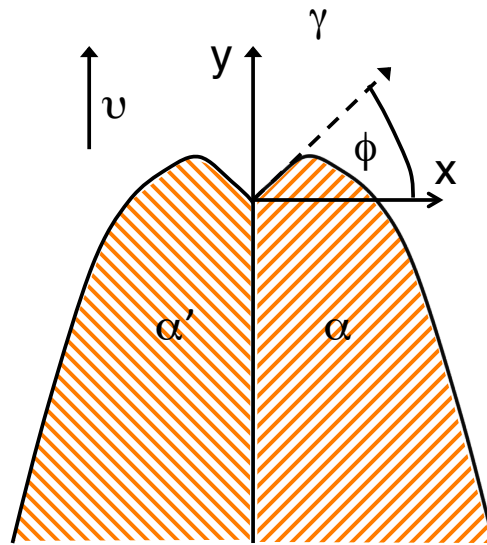
Figure 4. Steady-state bicrystal growth with velocity v **along the** y **axis. The kinetics is here limited by diffusion, and the geometry and propagation velocity are found by sharp interface methods. The angles defining the lattice strains as** $\epsilon_{xx}^0 = -\epsilon_{yy}^0 = \epsilon \cos 2\theta$, $u_{xy}^0 = \epsilon \sin 2\theta$ **are** $\theta = 2\pi/3$ **in the** α **phase and** $\theta = -2\pi/3$ **in the** α' **phase. For further details we refer to [53, 54]**

well as the strain ϵ_{ik}^α in the newly generated phase, which is related to the strain on the other side via the coherency and stress balance relations. Here, the eigenstresses σ_{ik}^0 are defined as $\sigma_{ik}^0 = 2\mu\epsilon_{ik}^0 + \lambda\delta_{ij}\epsilon_{kk}^0$. Additionally, similar to the discussion above, we have to provide thermal, elastic and phase boundary and initial conditions for the entire sample. For further details, we refer to [53].

The physical picture emerging from Eqs. (19)-(22) is clear: The propagation of the interface releases latent heat proportional to the normal component of the growth velocity v_n, while the local transition temperature itself depends on the elastic state at the interface and the curvature. The transport of the latent heat from the interface limits the propagation velocity.

In accordance with studies on displacive transformations, which are discussed above, we choose the hexagonal-orthorhombic transition here as example. Emerging bicrystal patterns, as they result in the steady state regime, are shown in Fig. 4. They are obtained from a sharp interface modeling for phase transformations in an infinite sample.

One of the central features of the elastic effects during solid state transformations is their strong influence on the growth velocities. In comparison to other diffusion limited processes e.g. during solidification, where elastic effects play only a minor role, they lead here to significantly higher transformation velocities. This experimentally well known phenomenon is correctly captured by the above model. Moreover, it is known that anisotropy is important for selection of the tip scale and the solidification velocity during dendritic growth. Here it turns out that the elastic anisotropies dominate
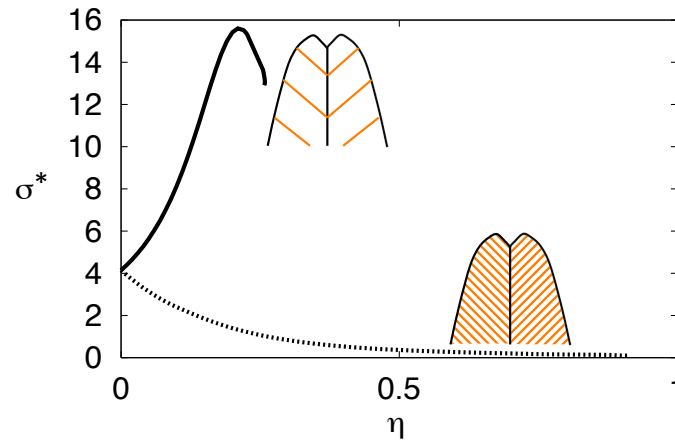
Figure 5. The velocity $\sim \sigma^\star$ of two steady-state transformation modes indicated by ϵ^+, ϵ^- which differ by the sign of the dilatational lattice strain relative to the shear lattice strain at fixed driving force. The dependence of both curves on the mixing parameter η exhibits the crucial influence of the relation of shear and dilatational strain.

the selection compared to the much weaker surface tension anisotropy effects, which therefore can be neglected here. It is therefore worthwhile to study the role of anisotropies of the transformation strain ϵ_{ij}^0 in more detail. Hence we use additionally the more complicated eigenstrain $\epsilon_{ik}^{0\pm} = (1 - \eta)\epsilon^s \pm \eta\epsilon_{ik}^d$ as a weighted superposition of a hydrostatic lattice strain $\epsilon_{ik}^d = \epsilon\delta_{ik}$ and the shear lattice strain ϵ_{ik}^s given by Eq. (7) with angles $\theta = 0, \pm 2\pi/3$. For $\eta = 1$ and $\eta = 0$ we recover the pure shear and pure hydrostatic stress free strains, respectively. η is therefore a measure for the deviatoric part of the eigenstrain. This model allows to consider the drastic influence of the orientation of lattice strains relative on the growth direction of the new phase. In Fig. 5 the eigenvalue $\sigma^* = d_0/p\rho$ of the steady state problem is shown as function of the mixing parameter η between the two types of mismatch strains. Here, p is the Peclet number and ρ the radius of the asymptotic Ivantsov parabola, see [55] for details. Therefore, the eigenvalue σ^* is a measure for the growth velocity, to which it is directly proportional at a fixed value of the driving force. We find a strong difference in the growth velocity for different orientations of the bicrystal microstructure. In fact, the growth velocity can easily differ by two orders of magnitude. Hence, the elastic anisotropy strongly affects the selection of the growth direction. Moreover, there is a strong dependence of the growth velocity on the type of transformation strain, and some steady state modes can only be found in a limited regime of the parameter η. Therefore, we can expect to find also discontinouos transitions between different microstructures.

At this point it should be pointed out that the sharp interface method allows to track also metastable solutions. Without that, it would not have been possible to track slower growth modes. In phase field simulations, in contrast, typically only the fastest growing mode will be found in the steady state regime, unless it is suppressed by suitable boundary conditions. In turn, this implies that the combination of phase field and sharp interface methods allows not only to find potential steady state patterns,
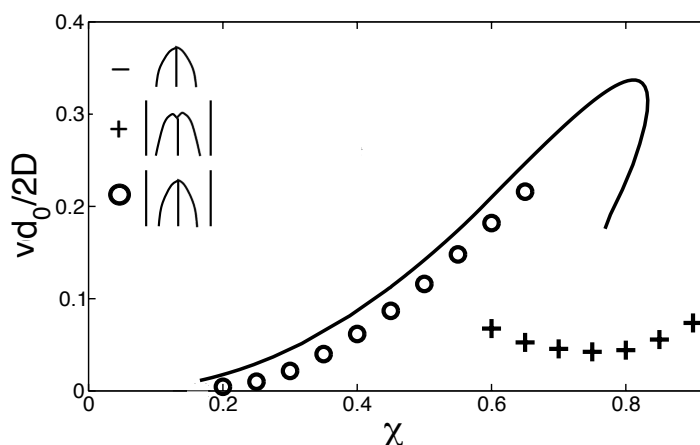
Figure 6. Comparison of growth velocities obtained from phase field model simulations of for a channel geometry (crosses and circles) and sharp-interface predictions for an infinite system (continuous curve). For the phase field simulations two different morphologies are anticipated. For the kinetically favoured one we find good agreement of the phase field simulations with the sharp interface theory. The mixing parameter $\eta = 0.1$ is fixed.

but also to decide about their stability. For that, we also have implemented a phase field formulation analogous to Eqs. (19)-(22). We refrain here from giving the model equations explicitly and refer to [53] instead. The phase field simulations can be compared to the sharp interface predictions in a regime of small widths of the transformation pattern relative to the (finite) width of the system. We note that the phase field simulations correspond to a finite-width channel geometry while the sharp-interface calculations use infinite systems. The comparison of phase field simulations and sharp-interface predictions in Fig. 6 shows excellent agreement. The obtained agreement for pattern widths relative to the channel size in the range from $\chi = 0.2 - 0.65$ is therefore very convincing concerning both the existence of steady transformation modes and their dynamical stability.

3.3. Phase field simulation of bainite formation

Based on the fundamental concepts discussed above, we generalize the description for the application to the austenite to bainite transformation. This involves the displacive deformation of the matrix, diffusion controlled growth of bainitic sheaves and the precipitation of carbides inside the ferrite (lower bainite) or inside the austenite (upper bainite). A successful prediction of the transformation kinetics requires consideration of the complex interaction of these processes: Elastic and plastic deformations, carbon partitioning and carbide precipitation. The local driving force for the transformation depends sensitively on the carbon concentration, stress tensor and temperature. During the transformation, the supersaturated carbon in the bainitic ferrite can either go to the surrounding austenite or the embedded carbides, which offer sites for the solute atoms. The multiphase field method proposed by Steinbach

et al. [56, 49] is most suitable for the simulation of such complex interactions. Here we briefly review the multi-order parameter phase field model and its application to the bainitic transformation of a high-carbon steel 100Cr6. For further details we refer to [26, 57, 27].

The starting point is the free energy of the system as a functional of the phase fields $\phi_\alpha(\vec{x}, t)$, the concentration field $c(\vec{x}, t)$ and the elastic strain field $\epsilon(\vec{x}, t)$,

$$F = \int_\Omega f(\phi, c, \epsilon) \, \mathrm{d}V = \int_\Omega \left[f^{\text{intf}}(\phi) + f^{\text{chem}}(\phi, c) + f^{\text{elast}}(\phi, \epsilon) \right] \mathrm{d}V, \tag{23}$$

where f^{intf}, f^{chem} and f^{elast} are the interfacial, chemical and elastic energy density, respectively. We use here order parameters ϕ_α to distinguish between the different phases and orientations. The energy densities are given by

$$f^{\text{intf}} = \sum_{\alpha,\beta=1,\alpha\neq\beta}^{N} \frac{4\gamma_{\alpha\beta}}{\xi} \left[\phi_\alpha \phi_\beta - \left(\frac{\xi}{\pi} \right)^2 \nabla\phi_\alpha \cdot \nabla\phi_\beta \right], \tag{24}$$

$$f^{\text{chem}} = \sum_{\alpha=1}^{N} \phi_\alpha f_\alpha(c_\alpha^i) + \tilde{\mu}^i (c^i - \sum_{\alpha=1}^{N} \phi_\alpha c_\alpha^i), \tag{25}$$

$$f^{\text{elast}} = \sum_{\alpha=1}^{N} \phi_\alpha \frac{(\epsilon_{ij}^\alpha - \epsilon_{ij}^{\alpha,0}) C_{ijkl}^\alpha (\epsilon_{kl}^\alpha - \epsilon_{kl}^{\alpha,0})}{2}. \tag{26}$$

The subscripts α, β and i are the indices of phase and chemical component, respectively. N is the number of phases. The interfacial energy density is defined by the double obstacle potential, which we use here instead of the double well potential described above. It contains two parameters, the interfacial width ξ and energy $\gamma_{\alpha\beta}$. The former is identical for all interfaces while the latter depends on the phase pair, misorientation and inclination of the interface, see below. $f_\alpha(c_\alpha^i)$ is the bulk free energy density of each phase. The elastic energy density is formulated based on the strain tensor ϵ_{ij}^α, the eigenstrain tensor $\epsilon_{ij}^{\alpha,0}$ induced by the transformation and the elasticity matrix C_{ijkl}^α. This generalizes the isotropic elasticity to arbitrary symmetries and also allows to take into account phase dependent elastic constants. The phase field and concentration field are subjected to the constraints of mass conservation,

$$\sum_{\alpha=1}^{N} \phi_\alpha = 1, \tag{27}$$

$$\sum_{\alpha=1}^{N} c_\alpha^i = c^i. \tag{28}$$

The diffusion potential $\tilde{\mu}^i$ [58] is introduced as a Lagrange multiplier for the second constraint. The evolution equations for the phase field and the concentration field are derived as [56, 58]

$$\dot{\phi}_\alpha = \sum_{\beta=1}^{N} \mu_{\alpha\beta} \left\{ \gamma_{\alpha\beta} \left[\phi_\beta \nabla^2 \phi_\alpha - \phi_\alpha \nabla^2 \phi_\beta + \frac{\pi^2}{2\xi^2} (\phi_\alpha - \phi_\beta) \right] + \frac{\pi}{\xi} \sqrt{\phi_\alpha \phi_\beta} \Delta g_{\alpha\beta} \right\}, \tag{29}$$

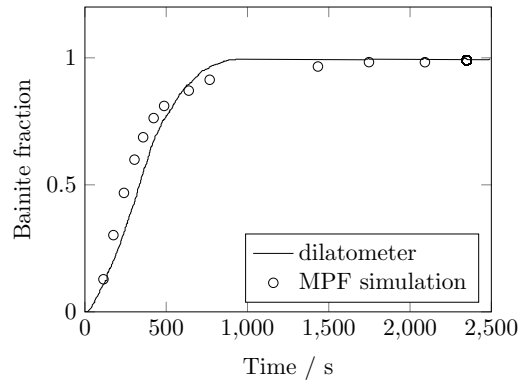$$\dot{c}_i^\alpha = \nabla \left(\sum_j D_\alpha^{ij} \nabla c_\alpha^j \right), \tag{30}$$

Figure 7. Comparison between the experimental and simulated kinetics of bainitic transformation in 100Cr6 (figure reproduced from [26]); The experimental and numerical data are determined by dilatometer measurements and MICRESS simulations, respectively.

where $\mu_{\alpha\beta}$ is the effective mobility defined for each phase pair. D_{ij}^{α} is the diffusion matrix in each phase, which is related to the chemical mobility matrix M_{ik} as $D_{ij}^{\alpha} = \sum_k M_{ik}(\partial^2 f_\alpha/\partial c^k \partial c^j)$.

The volume driving force $\Delta g_{\alpha\beta}$ comprises the differences of the bulk energy densities.

By assuming anisotropic interfacial mobility and tension we can reproduce the plate or needle like shape of the bainitic ferrite in the phase field simulations. As proposed in [26], both mobility and tension of the phase boundary are expressed as a function of the inclination θ, the angle between the interface norm and the facet norm,

$$\gamma_{\alpha\beta}(\theta) = \gamma_{\alpha\beta,0} k_{st,\alpha\beta}^2 (k_{st,\alpha\beta}^2 \cos^2\theta + \sin^2\theta)^{-3/2} \tag{31}$$

$$\mu_{\alpha\beta}(\theta) = \mu_{\alpha\beta,0}\left[k_{km,\alpha\beta} + (1 - k_{km,\alpha\beta})\tan\left(\frac{\kappa}{\tan\theta}\right)\frac{\tan\theta}{\kappa}\right], \tag{32}$$

where $\mu_{\alpha\beta,0}$ and $\gamma_{\alpha\beta,0}$ are prefactors of the interface mobility and tension, respectively. $k_{km,\alpha\beta}$ is the kinetic anisotropy coefficient and $k_{st,\alpha\beta}$ is the static anisotropy coefficient. κ controls the thickness-to-length ratio of the bainite sheave. See [26, 59] for a detailed discussion about the effects of each anisotropy parameter.

The application of the multi-order parameter phase field model to the bainitic transformation in 100Cr6 has been reported in our previous publications [26, 57, 27]. A commercial implementation of the multi phase field model, MICRESS (MICRostructure Evolution Simulation Software) [24] is employed. The free energy functions $f_\alpha(c_\alpha^i)$ of each phase are obtained from the Calphad database TCFe7 [60] using ThermoCalc. In Fig. 7 we show the results reported by Song et al. [26]. The experimental curve was determined by a dilatometer measurement, where the sample was austenized at 850°C, quenched to 260°C and then held isothermally. The corresponding simulation considered the diffusion controlled growth of the needle-shaped bainite. As shown in the figure, the volume fraction of bainite in the simulation agrees well with the measurement of the dilatometer.

To complement this approach, we apply a stress-coupled multi-phase-field-model in which the plate-like morphology results from the displacive essence of the transformation rather than the anisotropy of the interfaces. The deformation gradient tensor for the displacively transformed phase
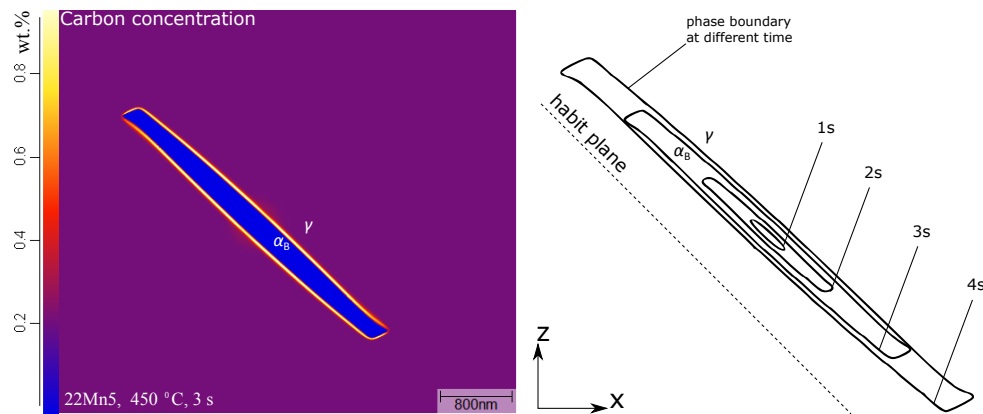
Figure 8. **Carbon distribution around a growing bainitic ferrite at 450 °C in steel 22Mn5(left), and the evolution of the ferrite/austenite phase boundary over time (right)**

is defined as $\boldsymbol{F} = \boldsymbol{I} + \vec{m} \otimes \vec{n}$. Here the vectors $\vec{m}$ and $\vec{n}$ denote the shear strain vector and the norm of the habit plane. The deformation gradient tensor is zero in the directions parallel to the habit plane and is an invariant-plane strain. To demonstrate the model, we run a simulation of the isothermal bainitic transformation of a carbon-manganese steel. The model is implemented in MICRESS, the equilibrium thermodynamic data for ferrite and austenite is calculated from the TCS steels/Fe-alloy database and the mass diffusion data from the TCS alloys mobility database. Due to the lack of plasticity, we scale down the transformation strain to 1/5 of the realistic value, which is 0.03 dilatational strain and 0.22 shear strain [61]. This prevents a premature frustration of the transformation due to artificially high elastic energy. The stress equilibrium is in agreement with a parallel-expansion boundary condition.

The results of stress-coupled multi phase field model are presented in Figs. 8 and 9. The visible domain in the figures is approximately 1/9 of the simulation domain. The stress arising from the elastic accommodation of the austenite matrix significantly affects the growth of the bainitic ferrite (α_B). Fig. 8 shows the evolution of the phase boundary and the partitioning of dissolved carbon during isothermal holding at 450°C. The growth of the bainite grain is constrained parallel to the habit plane by the trend of minimization of elastic energy in the matrix. The resulting stress field is shown in Fig. 9. The stress is certainly overestimated since the constitutive relation in this model is purely elastic. The simulated growth of bainitic ferrite is accompanied by carbon diffusion from the supersaturated ferrite to austenite, while substitutional elements, i.e. Cr, Si, Mn, are effectively frozen due to their low diffusivity. The bainitic ferrite exhibits partially a supersaturation of carbon.

Plastic effects on bainite formation, in particular under large external stresses, are not yet taken into account in the simulations, and this will be a future activity. Some open issues, which require to be understood on a mesoscale simulation level, are summarized in the next section.

3.4. Macroscopic description of transformation plasticity

The comparison of the multi-phase field simulations and the experiments have shown convincing agreement for 100Cr6 in several aspects. However, for applications of press hardening, where 22MnB5 is used, specifically anisotropic plastic response (transformation plasticity), remains to be incorporated
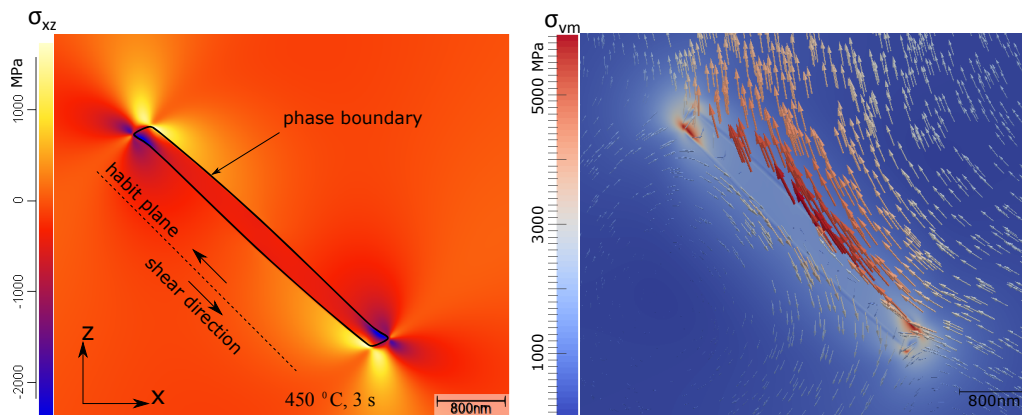
Figure 9. Stress distribution around a newly formed bainitic ferrite; (a) shear stress σ_{xz} in the undeformed configuration; (b) the von Mises stress in the deformed configuration where the the displacement field is indicated by arrows. Notice that plastic effects are not considered.

in future considerations. Here we give a short overview on this issue.

Transformation plasticity is meant to play a major role for bainitic transformations in partial press-hardening processes [41]. In Fig. 10 the simulated von Mises stress of a formed hat-profile of 22MnB5, shortly after the bainitic transformation has started, is shown. The simulation is started from an austenitized state, followed by a rapid cooling up to the process temperature (500°C). In the rounded edge regions the von Mises stress is significantly higher than the austenite yield strength of around 80 MPa. These findings suggest to develop an understanding of the material behavior and the kinetics of the bainite transformation under high stresses, i.e. higher than the yield strength, and also under the influence of pre-strain states.

On a macroscopic level, the transformation plasticity effect is modeled using a general approach [62]

$$\frac{d\epsilon_{ij}^{tp}}{dt} = \frac{3}{2} K S_{ij} \frac{df(p)}{dp} \frac{dp}{dt},\tag{33}$$

with K being the transformation plasticity constant, also known as Greenwood-Johnson parameter, S_{ij} a component of the deviatoric stress tensor, ϵ_{ij}^{tp} its corresponding transformation strain component and p the bainite volume fraction. $f(p)$ is a saturation function, which controls the transformation kinetics and operates in the range $[0, 1]$ both for the domain and values. Common approaches for the latter are given by Denis-Sjöström [63]

$$f(p) = p\,(2 - p)\,,\tag{34}$$

Leblond [64]

$$f(p) = p - p \ln p\tag{35}$$

and Tanaka [65]
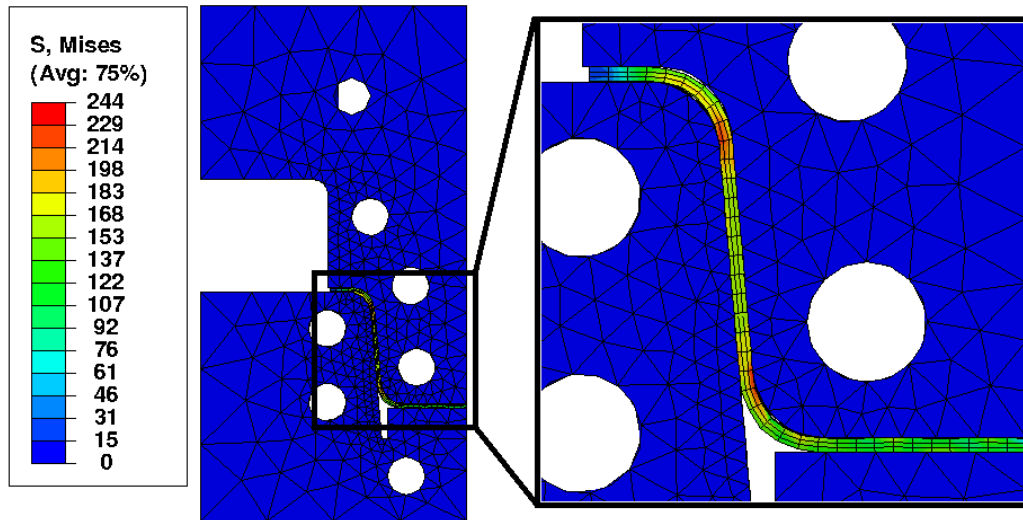
$$f(p) = p.\tag{36}$$

Figure 10. Von Mises stress distribution in MPa of a press-hardened hat profile of 22MnB5 at 500°C.

Integrating the expression (33) yields

$$\epsilon_{ij}^{tp} = \int\limits_{0}^{t} \frac{3}{2} K S_{ij}(\tau) \frac{d}{d\tau} f(p(\tau)) \, d\tau, \tag{37}$$

The diffusion-based phase transformation from austenite to bainite is described combining the models of Johnson, Mehl and Avrami (JMA) [37, 38] and Leblond [66]. This leads to the describing equation

$$\dot{p}(t, T, \dot{T}) = F(T, \dot{T})(\bar{p}(T) - p(t)) \frac{n(T)}{\tau(T)} \left[-\ln\left(1 - \frac{p(t)}{\bar{p}(T)}\right) \right]^{1 - \frac{1}{n(T)}}, \tag{38}$$

where $\bar{p}$ is the maximum phase fraction that can form at a given temperature, n and τ are temperature-dependent parameters controlling the transformation kinetics, and F is a correction function that takes into account the influence of the cooling rate on non-isothermal transformations. For the limit case of $\dot{T} = 0$, i.e. an isothermal transformation, $F(T, \dot{T} = 0) = 1$. This function must be experimentally determined; more detailed explanations can be found in [8].

In order to obtain values for the fit parameters n and τ, the effect of the applied stress on the bainitic transformation kinetics are studied experimentally. To understand the effect on the transformation behavior of an applied stress, several tests were performed in a servo-hydraulic deformation dilatometer Gleeble 3500. Flat tensile specimens are obtained from the sheet material by wire-cut electrical discharge machining with a total length of 120mm in accordance with ASTM E8/E8M-11 standard [67]. These tensile specimens were rapidly cooled down to 500°C after austenitization and were held at this temperature for 20 minutes. Shortly above this temperature a stress in the range of −20 to 200 MPa was applied. The temperature and load schedules utilized are illustrated in Fig. 11. The length and width changes of the specimens, in the L and T directions (see Fig. 11) respectively, are recorded by a laser extensometer. Finally, from the length change the kinetics of the bainite formation was calculated
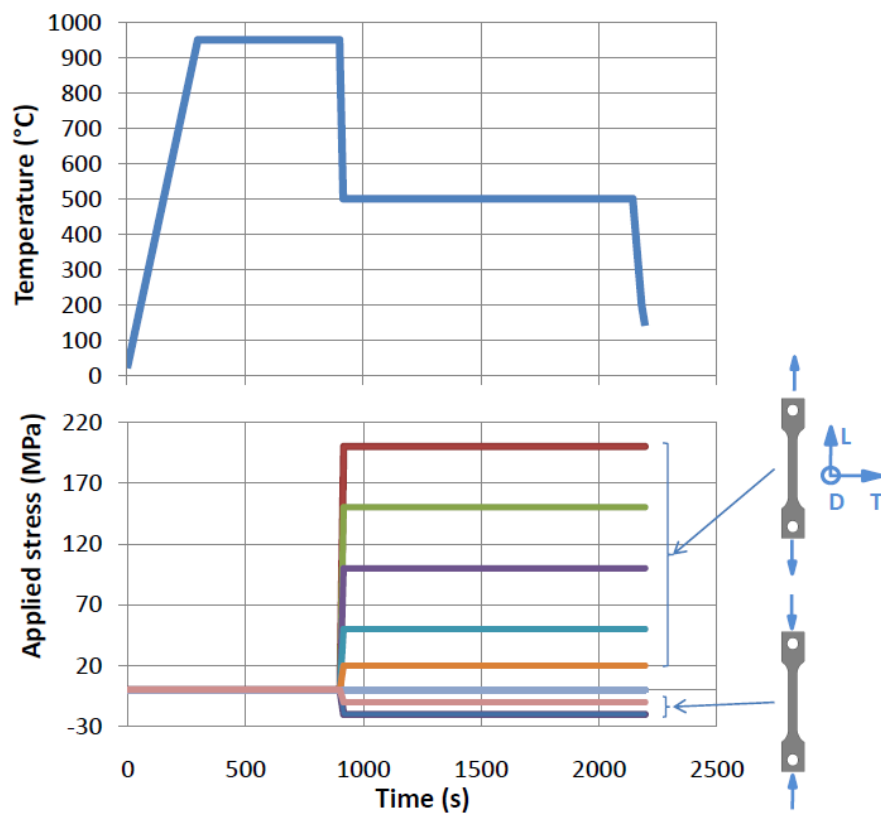
Figure 11. Form of thermomechanical treatment to study the stress affected bainitic transformation of 22MnB5.
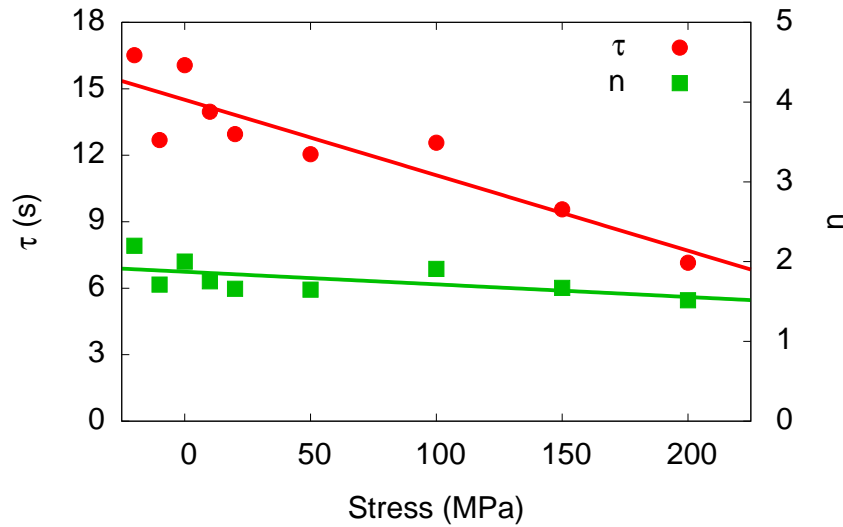
Figure 12. Johnson-Mehl-Avrami parameters at 500°C for the bainitic transformation under applied stress, see Eq. (38). The straight lines are linear fits to the data.

by fitting the above JMA equation. For these isothermal transformations, the bainite volume fraction evolution in time can be determined as

$$\frac{p(t)}{\bar{p}(T)} = \frac{l(t) - l_0}{l_{\max} - l_0},$$ (39)

with $l_0 = l_0(t_s)$ the length of the probe after the cooling to the transformation temperature and before the transformations has started, and l_{max} the length of the probe after the transformation has finished. The kinetic parameters $n(T)$ and $\tau(T)$ can the be determined from the relation [8]

$$\log\left[-\ln\left(1 - \frac{p(t)}{\bar{p}(T)}\right)\right] = n(T)\log\tau(T) - n(T)\log(t - t_s).$$ (40)

The results are presented in Fig. 12. It can be seen that whereas n remains practically constant, the parameter τ decreases approximately by a factor of 2 over the analysed stress range. This means that the time needed to complete the transformation for the case of the maximum applied stress in tension (200 MPa) is almost half the one for the compression case of -20 MPa.

From these tests another important effect can be observed when the transformation is performed under the influence of high stresses. This refers to the strong nonlinearity of the transformation plasticity or the anisotropic strain [68]. Such a behavior is not explained by the commonly used transformation plasticity models. In Fig. 13 the maximum measured anisotropic part of the length and the width strain after completion of the transformation are shown. The elastic and plastic strains due to the application of the external load are substracted, as well as the thermal strain up to the initiation of the bainitic transformation. During the tests, strains are measured both in longitudinal direction, ϵ_l, and in transversal direction, ϵ_t. Then, the volumetric transformation strain, ϵ_{tr}, is obtained as

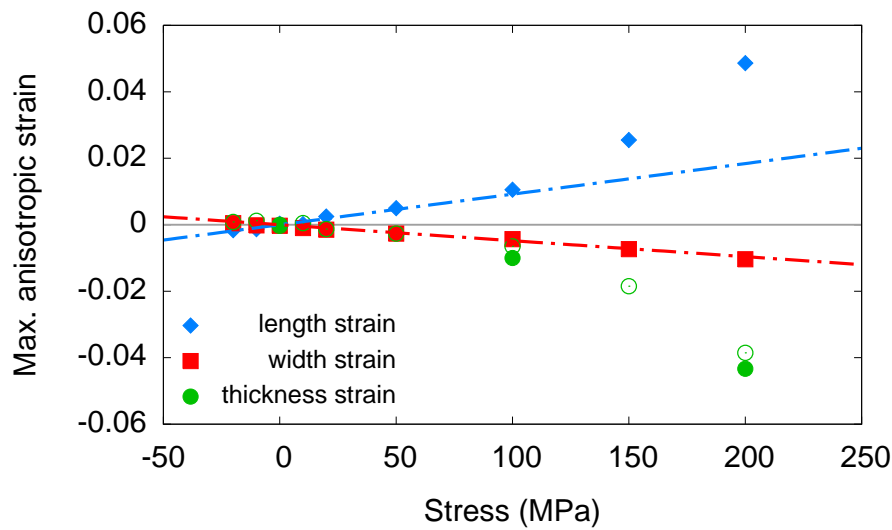$$\epsilon_{tr} = \epsilon_l + 2\epsilon_t.$$ (41)

Figure 13. Applied stress dependent anisotropic strain for the bainitic transformation. The straight lines are linearizations of the behavior near the origin, to highlight the pronounced nonlinearity of the length strain. In contrast, the width strain remains essentially linear. The thickness strain is consistently determined by two methods, i.e. using room temperature measurements (filled green circles) and from the volume change (empty green circles).

Considering a mean strain, we get the isotropic transformation strain

$$\bar{\epsilon}_{tr} = \frac{1}{3} \left(\epsilon_l + 2\epsilon_t \right) \tag{42}$$

the transformation-induced plastic strain in longitudinal direction is then given by the anisotropic longitudinal strain as

$$\epsilon_l^{tp} = \epsilon_l - \bar{\epsilon}_{tr}. \tag{43}$$

Similarly, for the transversal direction we get

$$\epsilon_t^{tp} = \epsilon_t - \bar{\epsilon}_{tr}. \tag{44}$$

From these results it can be seen that the length strain has a pronounced nonlinear response, whereas the width strain behaves linearly. In order to gain a better understanding, the thickness strain is calculated by two independent methods, first, from room temperature measurements and, second, from the volumetric strain. This data is also plotted in the figure. This way a similar behavior is observed for the thickness strain as for the length strain. The nonlinearity of the transformation plasticity starts in the range of 50-100 MPa, which can be explained by the fact that the austenite yield strength is reached or even exceeded during these tests.

The model of equation (33) gives a good approximation for the linear response of the transformation plasticity effect. The values of K for the tensile and compression cases have been determined as $K^+ = 11 \cdot 10^{-5} \, \mathrm{MPa}^{-1}$ and $K^- = 7.4 \cdot 10^{-5}, \mathrm{MPa}^{-1}$ respectively. However, to model the nonlinear response another model must be introduced [69, 70]. This aspect will be assessed in future works.

The experiments reveal that also another effect, namely the influence of pre-strained austenite, which is a consequence of the forming process, has substantial influence on the transformation kinetics. During the forming certain deformations can be reached in the austenitized component, even before the bainitic transformations starts. This topic is beyond the scope of the present paper, however, some initial results on this matter are reported in [71].

One of the main conclusions from the experimental observations is that applied stresses can accelerate the bainite formation during press hardening. It therefore remains an important task to understand this aspect also from a mesoscopic level, in particular using suitable extensions of phase field descriptions.

4. Conclusion

We have reviewed distinct approaches in the experimentally benchmarked modeling of different aspects of the bainite transformation during press hardening. To start with a basic thermodynamic model which allows to estimate the competitive behavior of different fundamental transformation morphologies, we have discussed combinations of sharp-interface and basic phase field models. The resulting insights about length scale and velocity regimes of appearing patterns in dependence of strain states and diffusional behavior of the material provides connections to multi phase field implementations, which are specifically adapted to the material data of 100Cr6 and 22MnB5. Taking into account also kinetic and surface stress anisotropies, simulations of the austenite-bainite transformation exhibit excellent agreement concerning the kinetics in the considered process regime with experimental data from scanning electron microscopy and dilatometric investigations. For the high stress regime, the conducted finite element simulations and the application of the Johnson-Mehl-Avrami model to 22MnB5 has allowed to extend these modeling approaches to the corresponding process regime. The results show a strong dependence of the plastic response on the applied stresses and the strain state of the material at austenitization. We note that a refined description of the coupling of nonlinear plastic response and the diffusional-displacive model is desirable for an advanced understanding of the later process regimes, especially for the austenite to bainite transformation in presence of a prestrain and high stresses.

Conflict of Interest

Authors state no conflicts of interest.

References

1. Smith CS (1960) A History of Metallography, University of Chicago Press.

2. Fielding L (2013) The bainite controversy. *Mater Sci Techn* 29:383–399.

3. van Bohemen S, Siemtsma J (2008) Modeling of isothermal bainite formation based on nucleation kinetics. *Int J Mat Res* 99:739–747.

4. Gaude-Fugarolas D, Jacques PJ (2006) A new physical model for the kinetics of the bainite transformation. *ISIJ Inter* 46:712–717.

5. Rees GI, Bhadeshia H (1992) Bainite transformation kinetics Part 1: Modified model. *Mater Sci Techn* 8:985–993.

6. Tzeng TC (2000) Autocatalysis in bainite transformations. *Mater Sci Eng A* 293:185–190.

7. Zolotoresvky N, Nesterova E, Titovets Y, et al. (2013) Modeling the effect of austenite deformation on the bainite structure parameters in low carbon microalloyed steels. *Int J Mat Res* 104:337–343.

8. Hunkel M, Lübben T, Hoffmann F, et al. (1999) Modellierung der bainitischen und perlitischen Umwandlung bei Stählen. *HTM Härterei-Techn Mitt* 54:365–373.

9. Quidort D, Brechet YJM (2002) A model of isothermal and non isothermal transformation kinetics of bainite in 0.5% C steels. *ISIJ Inter* 42:1010–1017.

10. Maier H-J, Ahrens U (2002) Isothermal bainitic transformation on low alloy steels: factors limiting prediction of the resulting material's properties. *Z Metallk* 93:712–718.

11. Freiwillig R, Kudrman J, Chraska P (1976) Bainite transformation in deformed austenite. *Metall Trans A* 7:1091–1097.

12. Holzweissig M, Canadinc D, Maier H-J (2012) In-situ characterization of transformation plasticity during an isothermal austenite-to-bainite phase transformation. *Mater Char* 65:100–108.

13. Su T, Veaus M, Aeby-Gautier E, et al. (2003) Effect of tensile stresses on bainitic isothermal transformation. *J Phys IV France* 112:293–296.

14. Su T, Aeby-Gautier E, Denis S (2006) Morphology changes in bainite formed under stress. *Scripta Mater* 54:2185–2189.

15. Hase K, Garcia-Mateo C, Bhadeshia H (2004) Bainite Formation influenced by large stress. *Mater Sci Techn* 20:1499–1505.

16. Kundu S, Hase K, Bhadeshia S (2007) Crystallographic texture of stress affected bainite. *Proc Royal Soc A* 463:2309–2328.

17. Fuijiwara K, Okaguchi S, Ohtani H (1995) Effect of hot deformation on bainite structure in low carbon steels. *ISIJ Inter* 15:1006–1012.

18. Min J, Lin J, Min Y, et al. (2012) On the ferrite and bainite transformation in isothermally deformed 22MnB5 steels. *Mater Sci Eng A* 550:375–387.

19. Nikravesh M, Naderi M, Akbari GH (2012) Influence of hot plastic deformation and cooling rate on martensite and bainite start temperatures in 22MnB5 steel. *Mater Sci Eng A* A 540:24–29.

20. Karbasian H, Tekkaya AE (2010) A review on hot stamping. *J Mat Proc Tech* 210:2103.

21. Feuser P, Schweiker T, Merklein M (2011) Partially hot-formed parts from 22MnB5 - process window. *ICTP Aachen* 10:408.

22. Chen L (2002) Phase fields models for microstructure evolution. *Annu Rev Mater Res* 32:113.

23. Wang Y, Jin YM, Khachaturyan AG (2004) The effects of free surfaces on martensite microstructures: 3D phase field microelasticity simulation study. *Acta Mat* 52:1039.

24. Micress microstructure evolution simulation software, `www.micress.de`.

25. Loginova I, Agren J, Amberg G (2004) On the formation of Widmanstätten ferrite in a binary Fe-C phase-field approach. *Acta Materialia* 52:4055–4063.

26. Song W, Prahl U, Bleck W, et al. (2011) Phase field simulations of bainitic phase transformation in 100Cr6. *Supplemental proceedings: Materials Fabrication, Properties, Characterization, and Modeling* 2:417–425.

27. Song W (2014) Characterization and simulation of bainite transformation in high carbon bearing steel 100Cr6, *PhD thesis RWTH Aachen University*.

28. Arif T, Qin R (2013) A phase field model for bainitic transformation. *Computational Materials Science* 77:230–235.

29. Arif T, Qin R (2014) A phase field model for the formation of martensite and bainite. *Advanced materials research* 922:31–36.

30. Qin R, Bhadeshia H (2009) Phase field model to study the effect of interface anisotropy on the crystal morphological evolution of cubic metals. *Acta Materialia* 57:2210–2216.

31. Bhadeshia H (1987) Worked examples in the geometry of crystals, *Institute of metals, London and Brookfield*.

32. Bouville M, Ahluwalia R (2006) Interplay between diffusive and displacive phase transformations: Time-Temperature-Transformation diagrams and microstructures. *Phys Rev Lett* 97:055701.

33. Kundin J, Raabe D, Emmerich H (2011) A phase field model for incoherent martensitic transformations including plastic accommodation processes in the austenite. *Journal of the mechanics and physics of solids* 59:2082–2102.

34. Kundin J, Pogorelov E, Emmerich H (2015) Numerical investigation of the interaction between the martensitic transformation front and the plastic strain in austenite. *Journal of the mechanics and physics of solids* 76:65–83.

35. Levitas V, Javanbakht M (2013) Phase field approach to interaction of phase transformation and dislocation evolution. *Applied Physics Letters* 102:251904.

36. Roters F, Eisenlohr P, Hantcherli L, et al. (2010) Overview of constitutive laws, kinematics, homogenization and multiscale methods in crystal plasticity finite element modeling: Theory, experiments, applications. *Acta Materialia* 58:2210–2216.

37. Johnson W, Mehl R (1939) Reaction kinetics in process of nucleation and growth. *Trans AIME* 135:416–458.

38. Avrami M (1941) Kinetics of phase change III: granulation, phase change and microstructure. *J Chem Phys* 9:177–184.

39. Lee G, Kim S, Han H (2009) Finite element investigations for the role of transformation plasticity on springback in hot press forming process. *Comp Mater Sci* 47:556567.

40. Hunkel M (2012) Anisotropic transformation strain and transformation plasticity: two corresponding effects. *Mat -wiss u Werkstofftech.* 43:150–157.

41. Lütjens J, Hunkel M (2013) The influence of the transformation plasticity effect on the simulation of partial press-hardening. *Proc 4th Int Conf CHS2* 319–327.

42. Brener EA, Marchenko VI, Spatschek R (2007) Influence of strain on the kinetics of phase transitions in solids. *Phys Rev E* 75:041604.

43. Fratzl P, Penrose O, Lebowitz JL (1999) Modelling of Phase Separation in Alloys with Coherent Elastic Misfit. *J Stat Phys* 95:1429.

44. Freund L (1998) Dynamic fracture mechanics, Cambridge University Press.

45. Spatschek R, Brener E, Karma A (2011) Phase field modeling of crack propagation. *Phil Mag* 91:75.

46. Chien FR, Clifton RJ, Nutt SR (1995) Stress-induced phase transformation in single crystal titanium carbide. *J Am Ceram Soc* 78:1537.

47. Spatschek R, Müller-Gugenberger C, Brener E A, et al. (2007) Phase field modelling of fracture and stress-induced phase transitions. *Phys Rev E* 75:066111.

48. Spatschek R, Eidel B (2013) Driving forces for interface kinetics and phase field models. *Int J Solid and Structures* 50:2424.

49. Steinbach I (2011) Phase field models in materials science. *Modelling and Simulation in Materials Science and Engineering* 17:073001.

50. Steinbach I, Shchyglo O (2011) Phase field modelling of microstructure evolution in solids: Perspectives and challenges. *Current opinion in solid state and materials science* 15:87.

51. Rao M, Sengupta S (2003) Nucleation of solids in solids: ferrite and martensite. *Phys Rev Lett* 91:045502.

52. Brener EA, Iiordanskii SV, Marchenko VI (1999) Elastic effects on the kinetics of a phase transition. *Phys Rev Lett* 82:1506.

53. Brener EA, Boussinot G, Hüter C, et al. (2009) Pattern formation during diffusional transformations in the presence of triple junctions and elastic effects. *J Phys Cond Mat* 21:464106.

54. Pilipenko D, Brener EA, Hüter C (2008) Theory of dendritic growth in the presence of lattice strain. *Phys Rev E* 78:060603.

55. Ivantsov GP (1947) PhD thesis Akad. Nauk. SSSR.

56. Steinbach I, Pezzolla F (1999) A generalized field method for multiphase transformations using interface fields. *Physica D: Nonlinear Phenomena* 134:385–393.

57. Song W, von Appen J, Choi P, et al. (2013) Atomic-scale investigation of epsilon and theta precipitates in bainite in 100Cr6 bearing steel by atom probe tomography and ab initio calculations. *Acta Materialia* 61(20):7582–7590.

58. Eiken J, Boettger B, Steinbach I (2006) Multi-phase-field approach for multi-component alloys with extrapolation scheme for numerical application. *Phys Rev E* 73:066122.

59. Steinbach I, Pezzolla F, Prieler R (1995) Grain selection in faceted crystal growth using the phase field theory. In: The 7th conference on on modeling of casting, welding and advanced solidification processes.

60. Lukas H, Fries S, Sundman B (2007) Computational thermodynamics: The CALPHAD method, Cambridge University Press.

61. Rees GI, Shipway PH (1997) Modelling transformation plasticity during the growth of bainite under stress. *Materials Science and Engineering A* 223:168–178.

62. Wolff M, Böhm M, Dalgic M, et al. (2008) Evaluation of models for TRIP and stress-dependent transformation behavior for the martensitic transformation of the steel 100Cr6. *Comput Mater Sci* 43:108114.

63. Denis S (1997) Considering stress-phase transformation interaction in the calculation of heat treatment residual stresses. Series: International Centre for Mechanical Sciences 368:293–317.

64. Leblond J, Deveaux JC (1989) Mathematical modelling of transformation plasticity in steels I: Case of ideal-plastic phases. *Int J Plasticity* 5:551–572.

65. Fisher FD, Sun QP, Tanaka K (1996) Transformation-induced plasticity. *Appl Mech Rev* 49:317364.

66. Leblond JB, Deveaux J (1984) A new kinetic model for anisothermal metallurgical transformation in steels including effect of austenite grain size. *Acta Metallurgica* 32:137146.

67. ASTM International standard test methods for tension testing of metallic materials (2011). Available from: `www.astm.org`.

68. Hunkel M (2009) Anisotropic transformation strain and transformation plasticity: two corresponding effects. *Mat -wiss u Werkstofftech.* 40(5-6):466–472.

69. Devaux J, Leblond JB, Bergheau JM (2000) Numerical study of the plastic behaviour of a low alloy steel during phase transformation. *Journal of Shanghai Jiaotong University* 3:206–212.

70. Zwigl P, Dunand DC (1997) A non-linear model for internal stress superplasticity. *Acta Materialia* 45(12):5285–5294.

71. Schicchi DS, Hunkel M (2015) Transformation plasticity effect during bainite transformation on a 22MnB5 Steel Grade. *IDE 2015, Bremen, Germany*.